Finescale Dual-Doppler Analysis of Hurricane Boundary Layer Structures in Hurricane Frances (2004) at Landfall

KAREN A. KOSIBA AND JOSHUA WURMAN

Center for Severe Weather Research, Boulder, Colorado

ABSTRACT

Two Doppler on Wheels (DOW) mobile radars collected fine-spatial-scale dual-Doppler data in the right-front quadrant and eye of Hurricane Frances (2004) as it made landfall near Stuart, Florida. A 5.7-km dual-Doppler baseline established a dual-Doppler domain south and east of Fort Pierce, Florida, encompassing a 5.5 km × 5.5 km horizontal area, with a grid spacing of 20 m, allowing for the resolution of subkilometer-scale horizontal structures and associated kinematics. Three-dimensional vector wind analyses of the boundary layer revealed the presence of linear coherent structures with a characteristic wavelength of 400–500 m near the surface that increased in size and became more cellular in shape with increasing height. Average horizontal perturbation winds were proportional to average total horizontal winds. Within the eye of the hurricane, the features lost linear coherency despite a high mean wind speed, possibly due to changes in stability. A slight decrease in the characteristic wavelength of boundary layer structures was documented as the winds cross the barrier islands east of Fort Pierce. Vertical flux of horizontal momentum caused by individual vortical structures was substantially higher than values employed in turbulence parameterization schemes, but the domain-wide average flux was substantially lower than that in individual structures, likely due to the transient nature of the most intense portions of the structures. Analysis of the turbulent kinetic energy (TKE) yielded values comparable to those reported in previous observational studies over the open ocean. However, there was substantial variability in TKE within the dual-Doppler domain, emphasizing the challenge in obtaining representative samples using non-3D measurements such as dropsondes.

1. Introduction

The hurricane boundary layer (HBL) contains linearly organized coherent structures that may influence hurricane intensity through the transport of momentum, heat, and water vapor throughout the HBL (e.g., Wurman and Winslow 1998, hereafter WW98; Morrison et al. 2005, hereafter M05; Foster 2005; Lorsolo et al. 2008, hereafter L08; Zhang et al. 2008, hereafter Z08; Kosiba et al. 2013b, hereafter K13b). It has been hypothesized that these linear structures are manifestations of secondary roll circulations embedded within the primary flow of the HBL with upward and downward branches (WW98; M05), the former associated with enhanced surface convergence, the latter causing downward transport of

relatively higher momentum air and, hence, greater wind-damage potential (WW98). These circulations transport turbulent kinetic energy (TKE), generated primarily by the strongly sheared environment of the HBL (Zhu 2008), within and out of the HBL. Obtaining detailed three-dimensional measurements of the small and quickly evolving structures in the HBL, particularly at landfall, is difficult. Flight level restriction of research aircraft, a long revisit time between passes, and the beamwidth of airborne radars complicate resolution of small-scale near-ground, quickly evolving structures in studies using airborne radar data. Dropsonde observations, which can sample the depth of HBL, provide one-dimensional measurements that may not fully represent the heterogeneous HBL. Nevertheless, finescale observations of the vertical structure of the lower HBL are critical to verify, and, if necessary, improve upon, the robustness of boundary layer and turbulent parameterization schemes used in numerical models.

WW98 first documented HBL coherent structures (HBLCS) during the landfall of Hurricane Fran (1995)

ᵈ Denotes Open Access content.

Corresponding author address: Dr. Karen A. Kosiba, Center for Severe Weather Research, 1945 Vassar Circle, Boulder, CO 80305.
E-mail: kakosiba@cswr.org

using high-resolution Doppler on Wheels (DOW; Wurman et al. 1997; Wurman 2001) data. They identified coherent vortical structures, which they identify as "rolls," that exhibited a horizontal wavelength of approximately 500 m within the lowest 500 m of the HBL. Their finest-scale data revealed perturbations from the mean horizontal wind that approached 20 m s^{-1} within the lowest 50 m above ground level (AGL). The coherent structures were notably absent inside the eye as it made landfall. Inland, however, where stronger winds existed (50 m s^{-1} at 1000 m AGL), the coherent vortical structures persisted. WW98 suggested that a threshold speed may be needed for roll vortex generation/maintenance and/or that the disintegrating eye had rendered the HBL convectively stable and thus potentially not conducive to HBLSs.

L08 examined the HBLCS characteristics in Hurricanes Isabel (2003) and Frances, also using finescale mobile radar data. To resolve structures with length scales of a few hundred meters, only data within 5.7 km of the radars were used in their analysis.[1] In both hurricanes, HBLCSs were evident throughout the depth of their analysis domains (up to 400–550 m AGL) and the structures exhibited characteristic horizontal wavelengths that ranged in size from 100 to 1000 m, with a mean wavelength of approximately 400 m, comparable to the results of the single-Doppler studies of WW98 and K13b. L08 document an increase in wavelength of the HBLCSs with height. The magnitude of the residual velocities ranged from ±6 m s^{-1}, which was substantially smaller than those documented by WW98 in Hurricane Fran, but comparable to the residual velocities of 4–6 m s^{-1} documented by K13b in Hurricane Rita (2005). It is likely that the subjective analysis employed by WW98 in Hurricane Fran was biased toward the largest departures from the mean flow, not representing the mean perturbation, thus accounting for the discrepancy in reported perturbation amplitude. However, the possibility that the perturbation velocities were stronger in the somewhat higher winds of Hurricane Fran cannot be excluded.

Analysis of coarser-resolution Weather Surveillance Radar-1988 Doppler (WSR-88D) data by M05 for Hurricanes Fran, Bonnie, and Georges revealed the presence of HBLCSs, which they identify as rolls, with a characteristic wavelength of ~1450 m aligned nearly parallel to the mean flow. Using the (velocity–azimuth display) VAD-derived winds, M05 estimated a roll-induced vertical momentum flux of 8 m^2 s^{-2}, which is 2–3 times larger than the momentum flux typically obtained from the standard downgradient turbulence parameterization schemes used typically in hurricane models. Z08 reported roll vortices with a mean wavelength of 900 m over the open ocean, observed by aircraft (and corroborated by satellite observations) during the Coupled Boundary Layers Air–Sea Transfer (CBLAST) experiment. Z08 also noted that although these structures were approximately aligned with the mean wind direction and contributed much less to the total momentum flux than was documented in M05. Because of the coarseness of the data, the larger, kilometer-scale wavelengths reported in M05 and Z08 were likely aliased to larger scales than the analyses of WW98, L08, and K13b. It is also possible that differences in the sampling height and analysis methods contributed to the observed differences in wavelength.

Recently, Lorsolo et al. (2010, hereafter L10) devised a method to calculate TKE from single-Doppler airborne radar data and applied this method to extract the TKE field from five different hurricanes over the open ocean. They found that the largest TKE values were primarily located within the eyewall (at or inside the radius of maximum winds) within the HBL. TKE values reaching 16 m^2 s^{-2} were documented along the inner edge of the radius of maximum winds in the HBL. Rogers et al. (2012) found a similar TKE distribution in their analysis of airborne radar data collected in three additional hurricanes. Even in the best cases, however, the TKE analyses of L10 and Rogers et al. (2012) did not extend much below 200 m AGL and the comparatively coarse resolution of the data (<350 m at 10-km range and <175 m at 5-km range from the radar) precluded analysis of the TKE generated by the subkilometer-scale HBLCSs (e.g., Carbone et al. 1985).

Comparisons between the radar-derived TKE and dropsonde TKE data taken during CBLAST well outside of the radius of maximum winds yielded good agreement (L10). Zhang et al. (2011) used flight level (~450 m AGL) in situ data over the open ocean to assess the TKE and momentum flux distribution as a function of hurricane wind speed and radial location. TKE and momentum flux were observed to increase with increasing wind speeds and were almost an order of magnitude larger in the eyewall compared to values obtained outside of the eyewall. For wind speeds near or exceeding 40 m s^{-1}, TKE values exceeded 10 m^2 s^{-2} and momentum flux values exceeded 1.5 m^2 s^{-2}. Spectral analysis revealed that the dominant eddy spatial scale in their eyewall analyses was between 500 and 3000 m. The extreme lower end of the spatial scale of these structures is similar in size to the HBLCSs analyzed by WW98, L08, and K13b.

---

[1] At 5.7 km the 1.5° radar beamwidth had spread to 150 m, so it is questionable if features less than 500-m scale were well resolved at this range or beyond.
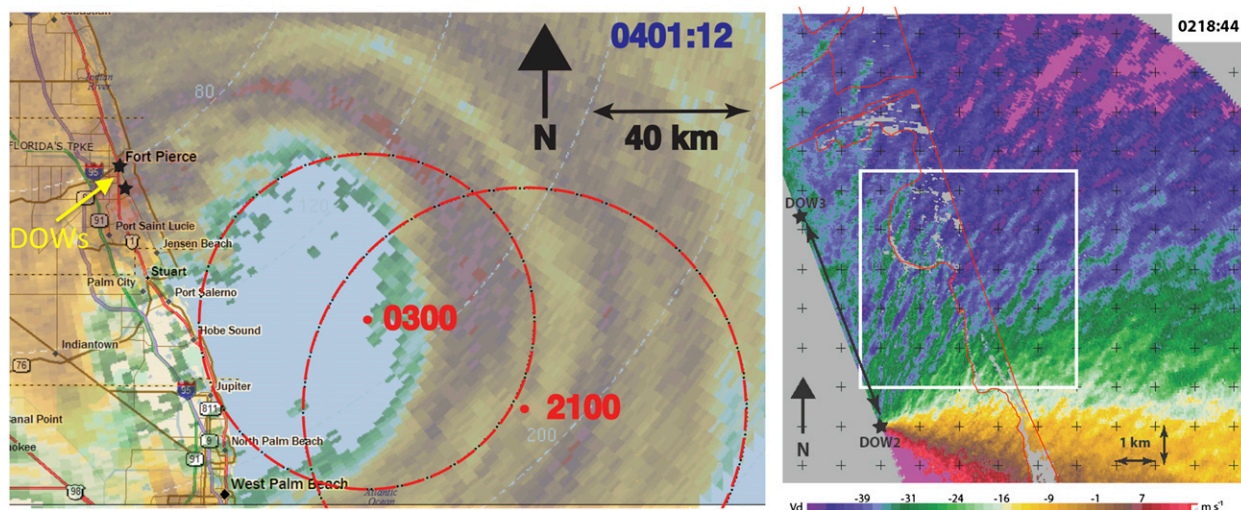
FIG. 1. Location of the DOW radars (black stars), during the landfall of Hurricane Frances on 5 Sep 2004. (left) Radar reflectivity measured by the Melbourne, FL, WSR-88D is shown at 0401:12 UTC, just after landfall. Note the high-reflectivity cell at the northwest edge of the eyewall, over Fort Pierce. Location of the approximate eye center is shown at both 2100 and 0300 UTC, along with the approximate boundary of the large eye. (right) Doppler velocity as measured by DOW2 radar near the time of landfall at 0218:44 UTC. The large dual-Doppler domain is the entire plotted area and the small dual-Doppler domain is outlined in white. Black stars indicate the location of the DOW radars and the location of the barrier island is outlined in red. Tick marks are at 1-km intervals.

Using the Weather Research and Forecasting Large-Eddy Simulation Model (WRF-LES) (e.g., Moeng et al. 2007), Zhu (2008) studied the effect of large eddy circulations (i.e., coherent boundary layer structures) on the turbulent transport within the HBL of landfalling Hurricane Ivan. Zhu (2008) concluded that the large eddy circulations contributed significantly to the total turbulent momentum and energy transport and proposed an updraft–downdraft model to assist in developing parameterization schemes. The TKE values retrieved by Zhu (2008) exceeded those reported in L10, likely because much of the TKE reported in Zhu was due to small-scale features that were unresolved (or under resolved) in the analyses of L10.

Analysis of finer-scale HBL vector wind fields is necessary to quantify accurately the TKE budget in the HBL due to HBLRs over a range of spatial scales. As hurricane models are particularly sensitive to the boundary layer parameterizations (e.g., Braun and Tao 2000; Hill and Lackmann 2009; Kerpert 2012), it is imperative to quantify the three-dimensional finescale HBL vector wind structure in order to develop parameterizations that account for the likely appreciable HBLCS contribution to the TKE and momentum flux. Analysis of very finescale resolution dual-Doppler data collected by the DOW radars in Hurricane Frances provide the best opportunity to date to examine the finescale three-dimensional vector wind structure and kinematics of the small-scale coherent features within the lowest levels of the HBL.

2. Description of data

Hurricane Frances made landfall with the center of the eye crossing the southern end of Hutchinson Island, Florida, at approximately 0430 UTC 5 September 2004 rated as a category 2 hurricane (Franklin et al. 2006). Two DOW radars (DOW2 and DOW3) were deployed by 1450 UTC 4 September, approximately 15 h ahead of landfall. DOW3 was deployed just south of Fort Pierce, Florida, at 27.44027°N, 80.32078°W and DOW2 deployed farther south at 27.39226°N, 80.3044°W (Fig. 1). Both DOW sites were immediately west of the bay behind Hutchinson Island, within 3 m horizontally of the water line, providing unobstructed views over the bay and barrier islands. The centers of the DOW antennas were approximately 4–6 m above sea level, which varied during landfall due to an approximately 2-m storm surge. The distance between the two DOW radars was 5.7 km, permitting some of the finest-ever-scale dual-Doppler syntheses in the HBL.[2] The dual-Doppler lobe encompassed the right-front quadrant of the hurricane eyewall as it made landfall; allowing for dual-Doppler vector wind syntheses in rainbands, eyewall, and, at the

---

[2] A triple-Doppler DOW array with baselines from 4–9 km was established over the Atlantic, sea level, and the Cedar Island Causeway, North Carolina, during the landfall of Hurricane Isabel (2003), and a very small triple-Doppler DOW array with baselines ranging from 1.0–2.7 km was established by deploying on levees near Point a la Hache, Louisiana, during the landfall of Hurricane Isaac (2013) (Wurman et al. 2013).

TABLE 1. Analysis interval, number of three-dimensional dual-Doppler syntheses, and location of the dual-Doppler domain and approximate distance of the domain from the center of the hurricane eye (km). Front right (FR) and right (R).

Analysis interval (UTC)	No. of dual-Doppler volumes	Quadrant	Distance from eye center (km)
2306–2326	11	FR	110
0000–0006	4	FR	108
0114–0116	2	FR	90
0136–0140	3	FR	80
0208–0218	5	FR	67
0340–0346	3	FR	47
0354–0358	2	FR	47
0402–0404	2	FR	43
0518	1	R	36

end of the analysis, inside the eye (Table 1).[3] Additionally, a north, northwest–south, southeast-oriented barrier island, roughly parallel to the mainland coastline and the DOW baseline, transects the domain (Fig. 1), affording the opportunity to examine the impact of the barrier island on roll morphology. This study focuses on characterizing the finescale, three-dimensional velocity structure of the HBL in the 6 h leading up to and including landfall from approximately 2300 UTC 4 September to 0500 UTC 5 September.

In 2004, DOW2 and DOW3 were single-polarization, single-frequency systems operating near a frequency of 9.37 GHz with peak transmit power of 250 kW (Wurman 2001). During the study period, pulse length and gating of 0.166 μs were matched to produce 25-m range resolution. The half-power beamwidth of 0.93° was oversampled in azimuth by about a factor of 3, producing radar samples spaced azimuthally every 0.3°. Radar sample volumes were thus 25 m $\times$ 80 m $\times$ 80 m = 160 000 m^3, oversampled to 25 m $\times$ 30 m $\times$ 80 m = 60 000 m^3, in the center of the dual-Doppler domain. Volumetric scanning from 0.5° to 6.8° elevation typically required 120 s. From 2300 to 0300 UTC, the dual-Doppler volume scan times between the two DOWs were synchronized to within 5 s, but after ~0300 UTC, the sync interval between the dual-Doppler volumes was as large as 60 s, possibly increasing synthesis errors due to temporal evolution. Between 2306 and 0518 UTC, 33 independent dual-Doppler grids were created for analysis.

Initially two dual-Doppler domains (Fig. 1b), of different size and grid spacing, were chosen in order to examine the properties and kinematics of the coherent

structures at very fine-spatial-scale resolution and at somewhat coarser scales dictated by radar resolution at ranges of a few kilometers to several kilometers in order to examine the wind structure through a deeper vertical domain. Radar data were interpolated to Cartesian grids using a two-pass Barnes scheme (Barnes 1964; Koch et al. 1983) with a second-pass convergence parameter γ of 0.30 (Majcen et al. 2008) similar to that used in studies of finescale structures in tornadic convective systems (e.g., Kosiba et al. 2013a). To account for the motion of features between consecutive scans, a translation adjustment was applied to the data based on the motion of coherent features, as determined through the minimization of the root-mean-square distance between features in consecutive volume scans. The large (small) domain was $X = Y = 12.0$ (5.5) km in the horizontal and $Z = 0.8$ (0.4) km in the vertical. The fine-spatial-scale small domain composes only the lowest portion of the HBL, while the large domain composes almost the entire depth of the HBL. The objective analysis parameters were chosen based on the azimuthal δ_h and vertical δ_v radar data spacing near the farthest edges of the dual-Doppler domains. For the large (small) domain, a conservative slightly oversampled interval of 0.7° and an elevation interval of 1° at a range of 8 (4) km resulted in $\delta_h = 110$ (49) m and $\delta_v = 157$ (70) m. A smoothing parameter [$\kappa = (1.33\delta)^2$] of 0.040 (0.017) km^2 (Pauley and Wu 1990) and horizontal and vertical grid spacing ($\Delta \sim \delta/2.5$) of 40 (20) m and 50 (25) m, respectively, were chosen (Koch et al. 1983). No downward extrapolation was employed in the objective analysis. These parameters allowed for 70% (91%) of the energy to be resolved for a 500-m wavelength in the analysis domain.

Vertical velocities w were derived from upward integration of the mass continuity equation using unfiltered horizontal velocities with a lower boundary condition of $w = 0$ m s^{-1} at $z = 0$ m above radar level (ARL).[4] Although there is large-scale vertical motion in a hurricane, small-scale fluctuations are likely to dominate, particularly below 500 m ARL. Dual-Doppler fields were extrapolated downward from the lowest observed level (~50–75 m ARL at the center of the domain) using downward propagation of the coefficients of the directional cosine terms of the dual-Doppler equation and iteratively solving for u, v, and w (see Kosiba et al. 2013a), where u and v are the horizontal

---

[3] The large hurricane eye was approximately 83 km in diameter at 0300 UTC and had a translation motion of approximately 2 m s^{-1}.

[4] ARL and above sea level and AGL are nearly indistinguishable for the purposes of this paper since the radar antennas were ~5 m above sea level, and the terrain over the barrier islands was fairly flat. Since some of the domain is above water, and some is above land, and the land–sea boundary varied in very low areas during the landfall due to surge, ARL is used in this paper.
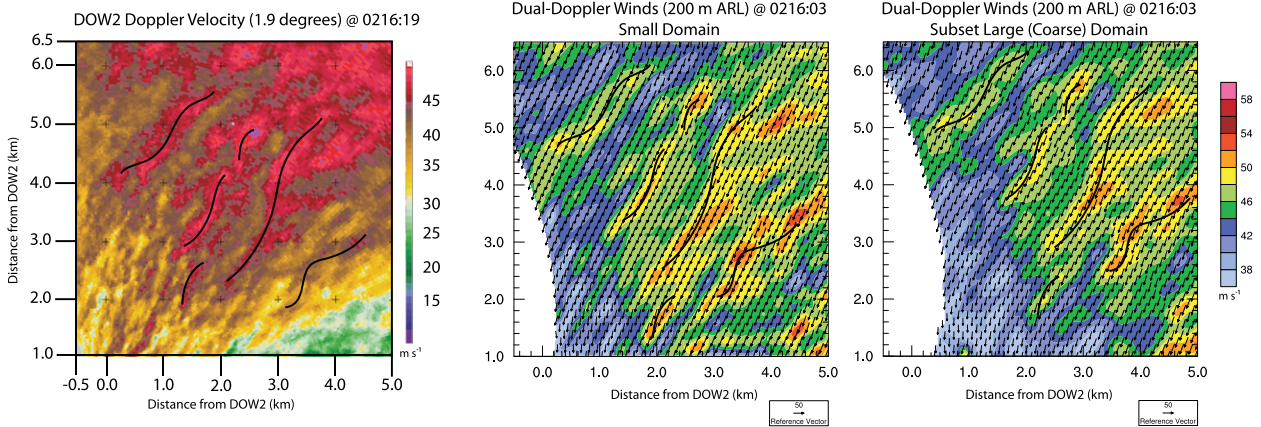
FIG. 2. Comparison of the magnitude of the (left) raw Doppler velocity data to (middle) the dual-Doppler synthesis in the small domain and (right) a subset of large coarser domain corresponding to the small domain at 0216 UTC. Solid black wavy lines indicate peaks in Doppler velocity and dual-Doppler horizontal wind speed associated with the wind streaks. (A translation correction is applied to the Doppler velocity so that the dual-Doppler syntheses are conducted at a common time, resulting in a spatial offset of the features between the two plots. Horizontal and vertical axes are distances east and north from DOW2 in kilometers.)

winds in the x and y directions, respectively. Horizontal perturbation velocities were determined by subtracting the mean horizontal winds, as determined from a horizontal domain average, at vertical grid level.

Comparisons between the radar-measured winds and the dual-Doppler horizontal wind syntheses from the small and large domains at 100 m ARL at times when the flow is approximately parallel to the DOW2 radar beam show that the structures present in the raw radar Doppler velocity data are preserved well in the dual-Doppler analyses (Fig. 2). Since the objective analysis parameters used for the smaller, finer-scale domain preserves the smaller-scale structures better than those used in the large domain and the wind field in the small domain is representative of the larger areal wind field, the analyses presented herein utilizes the small domain.

speed in the x direction and v is the speed in the y direction] and the standard deviation of the horizontal wind speed $[\bar{s} = (\overline{u'^2} + \overline{v'^2})^{1/2}$, where u' is the perturbation speed in the x direction and v' is the perturbation speed in the y direction] are positively correlated $[r = 0.73\ (0.70)$ at $z = 100\ (400)$ m ARL], though the signal is noisy (Fig. 3), suggesting that HBLCS intensity depends on background wind strength. Coherent structures in the total and perturbation horizontal wind fields are evident throughout the entire analysis period. From 2306 to 0218 UTC, these structures have a predominantly linear shape at low levels (Figs. 4 and 5) and then become more cellular in shape at approximately 400 m ARL (Fig. 6). From 0340 to 0402 UTC, as the inner eyewall and eye encroach into the analysis domain, the structures exhibit less linear morphology even at low

3. Analyses and results

a. Description of dual-Doppler winds

From 2306 to 0218 UTC, the winds in the dual-Doppler domain are associated with the HBL of the inner ($\leq$100 km from the center of the ~80-km diameter eye) rainbands. After 0218 UTC, there is a gap in the dual-Doppler coverage (Table 1) and beginning with the next analysis time, 0340 UTC, the dual-Doppler domain is at the edge of the eyewall. At 0354 UTC, a high-reflectivity convective cell along the edge of the eyewall rotates into the analysis domain and remains within the domain through the 0402 UTC (Fig. 1). The last dual-Doppler volume, 0518 UTC, was obtained inside the very large hurricane eye.

From 2306 to 0218 UTC, the domain-average total horizontal wind speed $[\bar{S} = (\overline{u}^2 + \overline{v}^2)^{1/2}$, where u is the

FIG. 3. Total (dashed) and perturbation (solid) average horizontal wind speed as a function of dual-Doppler analysis time at $z = 100$ m (blue) and $z = 400$ m (red).

Z = 100 m ARL
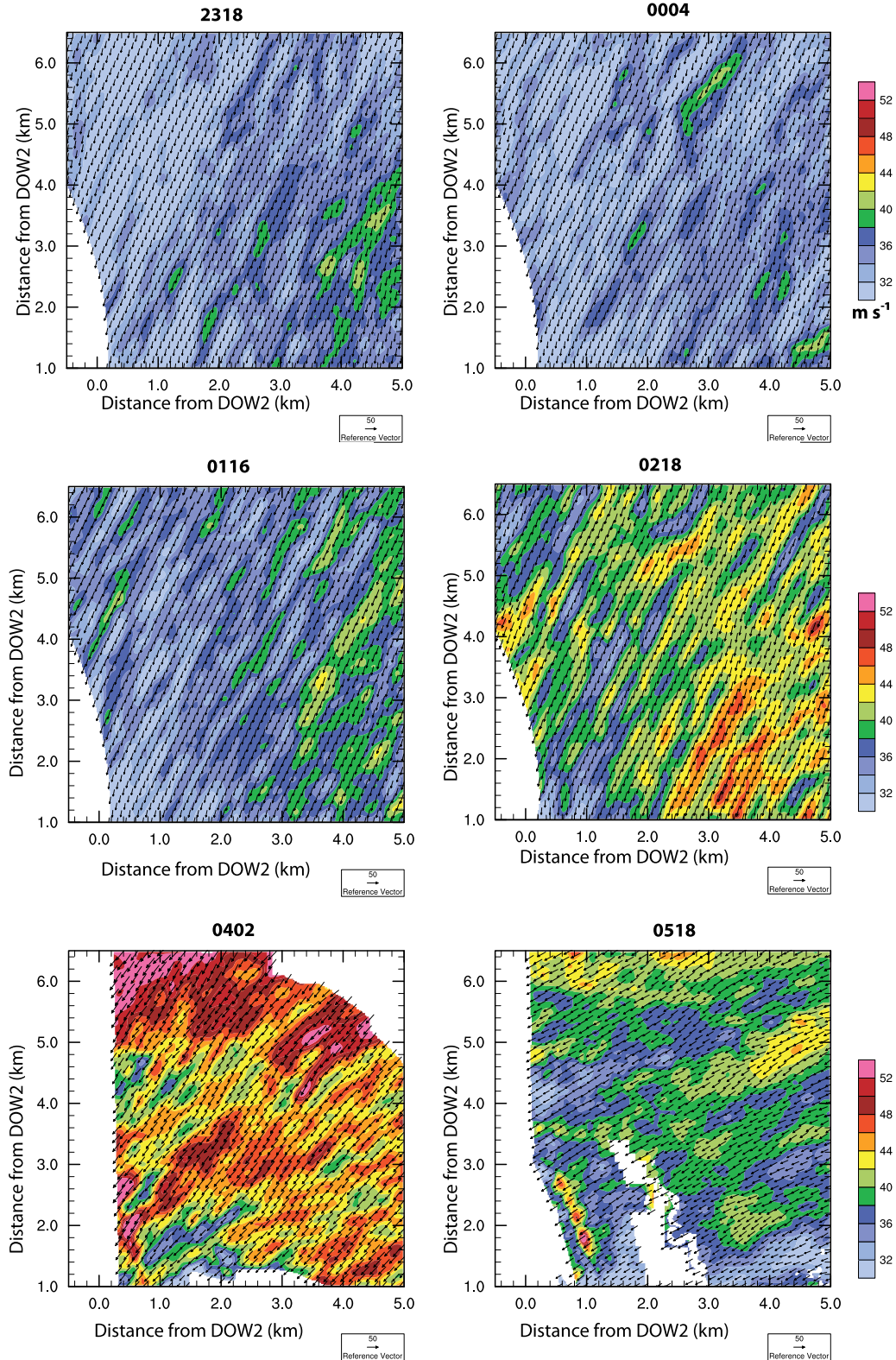
FIG. 4. Dual-Doppler horizontal winds (vectors) shown at representative times (UTC) during the analysis at $z = 100$ m ARL. Total horizontal wind speed is color contoured from 32 to 52 m s^{-1} in 2 m s^{-1} intervals.

Z = 100 m ARL
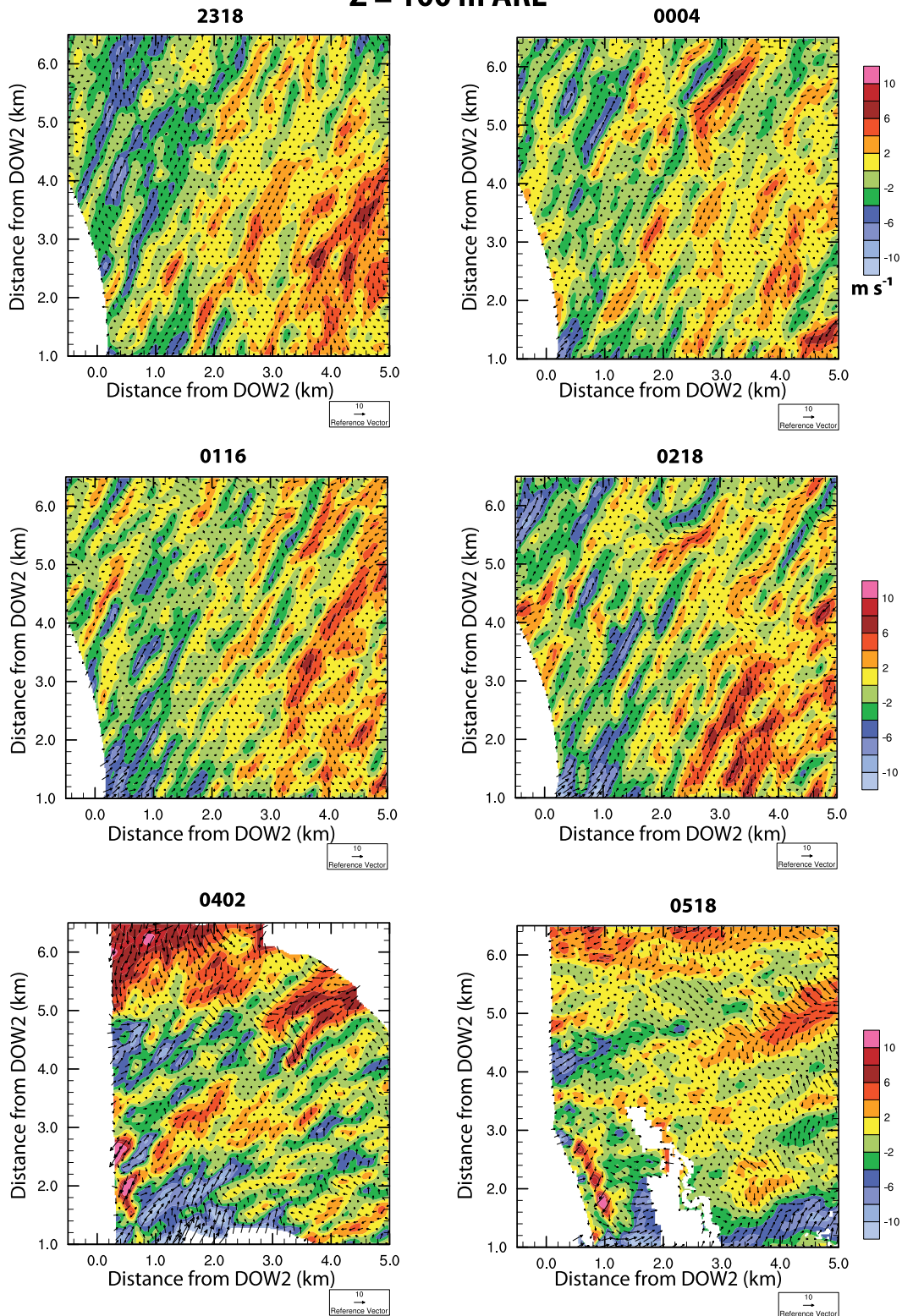
FIG. 5. Dual-Doppler perturbation horizontal winds (vectors) shown at representative times (UTC) during the analysis at $z = 100$ m ARL. Perturbation horizontal wind speed is color contoured from -10 to 10 m s^{-1} in 2 m s^{-1} intervals.

Z = 400 m ARL

2318   0218
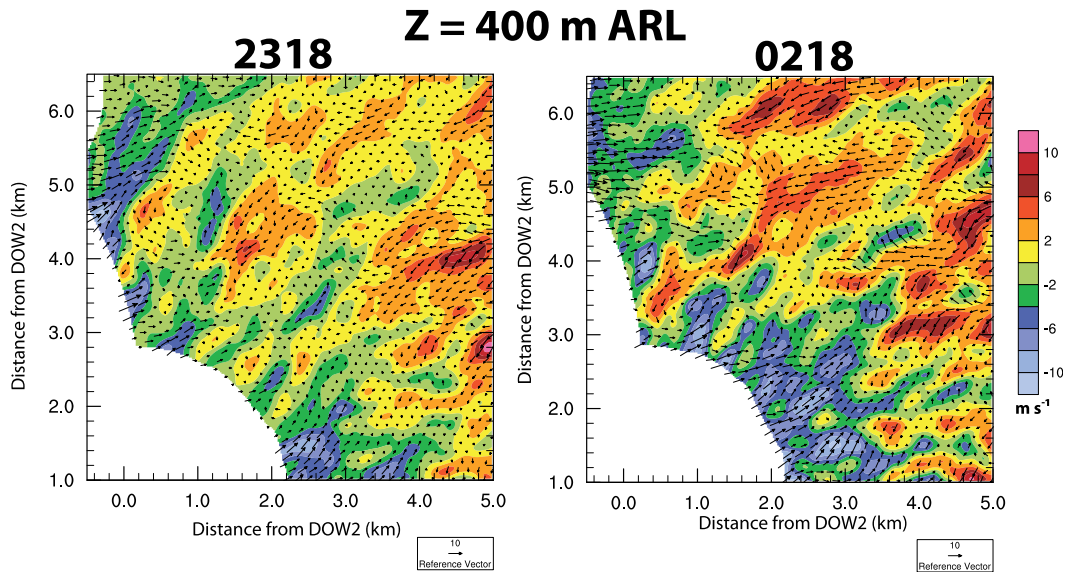
FIG. 6. Dual-Doppler perturbation horizontal winds (vectors) shown at 2318 and 0218 UTC at $z = 400$ m ARL. Perturbation horizontal wind speed is color contoured from -10 to 10 m s^{-1} in 2 m s^{-1} intervals.

levels (Figs. 4 and 5) compared at earlier times and, by 0518 UTC, the structures appear more amorphous. Since the total horizontal wind speeds were largest between 0340 and 0359 UTC, the generation/existence of rolls is not dependent only on wind speed, and must depend on HBL stability or other factors.

Vertical cross sections perpendicular to the axis of the coherent structures at 2318 and 0218 UTC show upward and downward motion through the depth of the domain (Fig. 7). Distinct downdrafts and updrafts are associated with some of the linear HBLR features, and there is a consistent domain-wide correlation ($r = -0.25$ to -0.36)
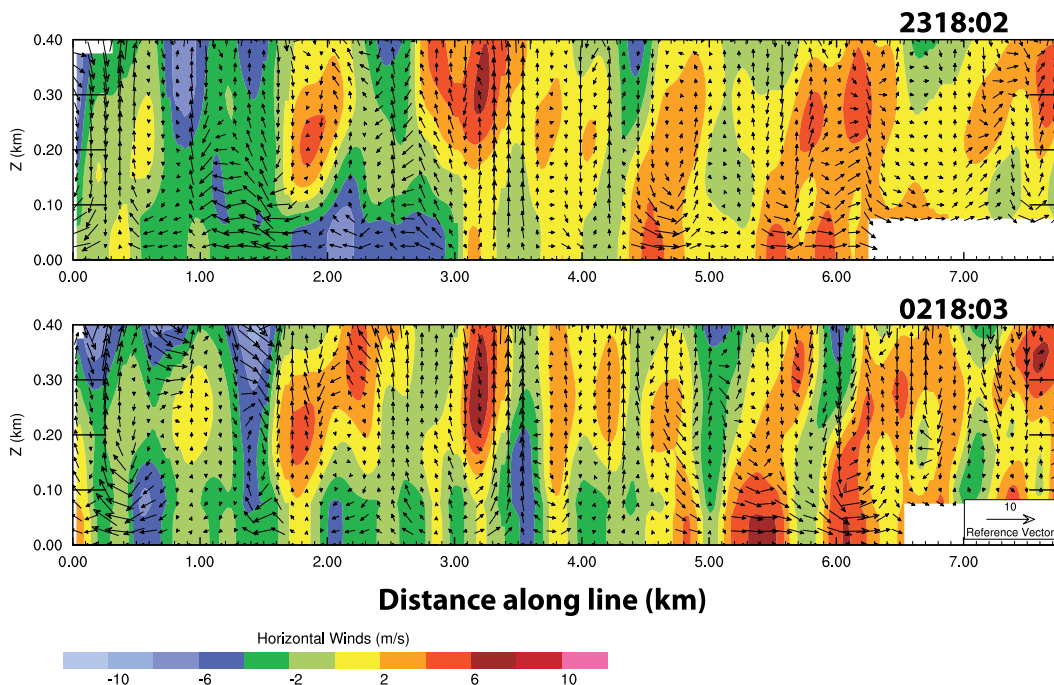
FIG. 7. Vertical cross sections of the dual-Doppler winds at (top) 2318:02 and (bottom) 0218:03 UTC. Color contours indicate the horizontal wind speeds into (blue) and out of (red) the cross-sectional plane, which is perpendicular to the long axis of the rolls, and vectors depict the perpendicular and vertical wind components.

0107:05
1 degree
0107:36
1 degree
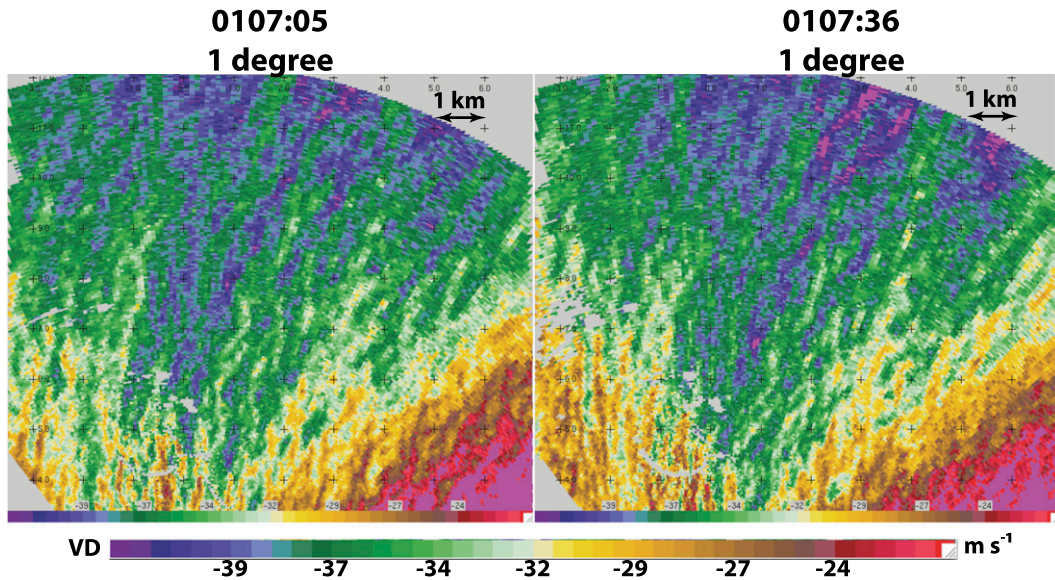
FIG. 8. The Doppler winds at 1° elevation at 0107:05 UTC and then 31 s later at 0107:36 UTC. Small-scale features evolve significantly during the 21-s interval, which is much less than the time required for a radar volume scan.

between horizontal perturbation wind speed and vertical motion. Since dual-Doppler vertical wind retrievals are particularly sensitive to a multitude of sampling limitations (e.g., upper/lower boundary conditions, storm evolution between consecutive scans, and nonexact simultaneity between sampling of a location by one DOW and the next), it is likely that the domain-wide correlation between horizontal perturbation winds and
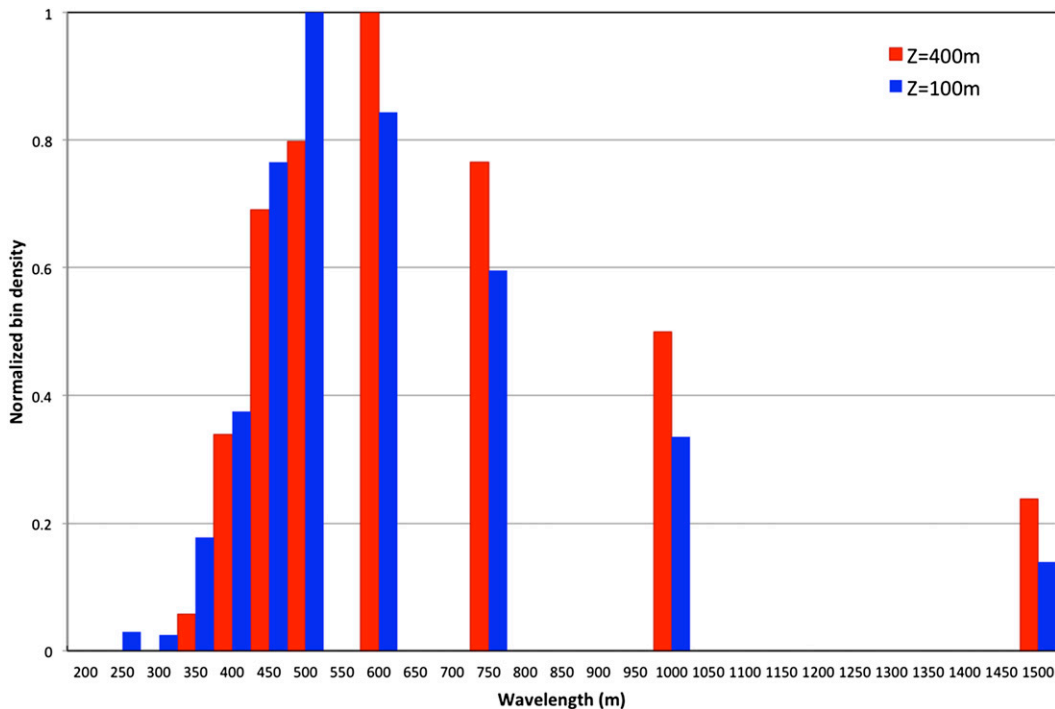
FIG. 9. Distribution of wavelength present in the dual-Doppler wind syntheses for all dual-Doppler times at $z = 100$ m ARL (blue) and $z = 400$ m ARL (red) using an FFT analysis. At $z = 100$ (400) m ARL, the most frequently occurring wavelength was 499 (610) m.
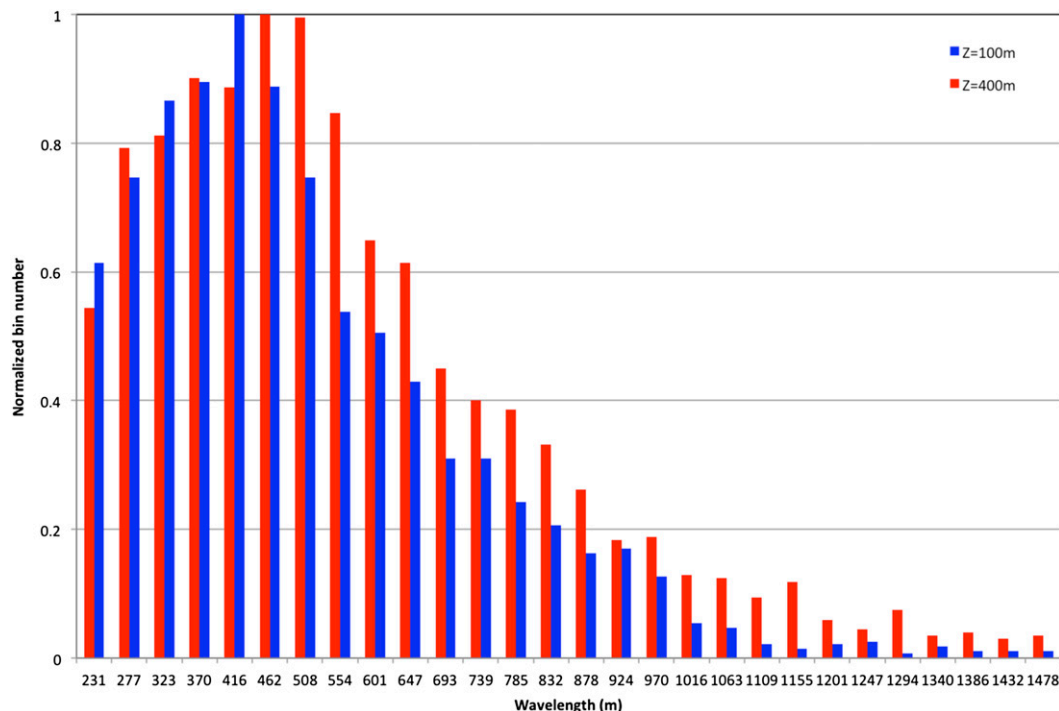
FIG. 10. Distribution of wavelength present in the dual-Doppler wind syntheses for all dual-Doppler times at $z =$ 100 m ARL (blue) and $z = 400$ m ARL (red) as determined by the peak-to-trough method. At $z = 100$ (400) m ARL, the most frequently occurring wavelength was 428 (462) m.

vertical winds was smaller than actuality due to errors in the vertical wind retrieval. Although the objective analysis methods account for the translation of small-scale features, some intense Doppler wind perturbations, likely associated with substantial updrafts and downdrafts, are seen to evolve significantly during periods much less than the radar volume scan interval (Fig. 8). These transient features are poorly sampled in individual radar sweeps, which may occur at slightly different times during the features' evolution. The mixture of steady and unsteady features, the latter sampled at varying periods in their evolution, in these analyses likely reduce the domain average correlation coefficients, impacting calculations of TKE and vertical fluxes of momentum, discussed below.

b. Characteristics

1) CHARACTERISTIC WAVELENGTH AND PERTURBATION SPEED

Since the finescale single-Doppler analyses of L08 and K13b revealed coherent structures with wavelengths less than 500 m, it was necessary to ensure that the dual-Doppler analyses adequately preserved these same small-scale features. Two different methods were employed to objectively characterize the wavelength of the

coherent features: a fast Fourier transform (FFT)[5] and a peak-to-trough wavelength statistical analysis. Using two different methodologies allowed increased confidence that analysis method bias was not causing misinterpretation of the data. For each dual-Doppler synthesis from 2306 to 0218 UTC, the characteristic wavelength of the residual wind speeds were analyzed along lines perpendicular to the long axis of the HBLCSs equally spaced (every 0.5 km) throughout the domain.[6] The analyses were calculated at heights of 100 m and 400 m ARL in order to assess any height dependency on the scale of the rolls.

To focus on the subkilometer-scale features and following the methodology of K13b, the three highest energy wavelengths at or below 1500 m were retained in the FFT and peak-to-trough analyses. The peak-to-trough method was similar to the analysis method of L08 in which the wavelength is determined by extracting the horizontal distance between successive peaks and troughs in the perturbation velocity and then multiplying

---

[5] The one-dimensional spatial FFT decomposed the perturbation speed signal into a series of wavenumbers associated with a particular power. Wavenumbers were converted to discrete wavelengths.

[6] The number of lines for each time varied as a function of data coverage.
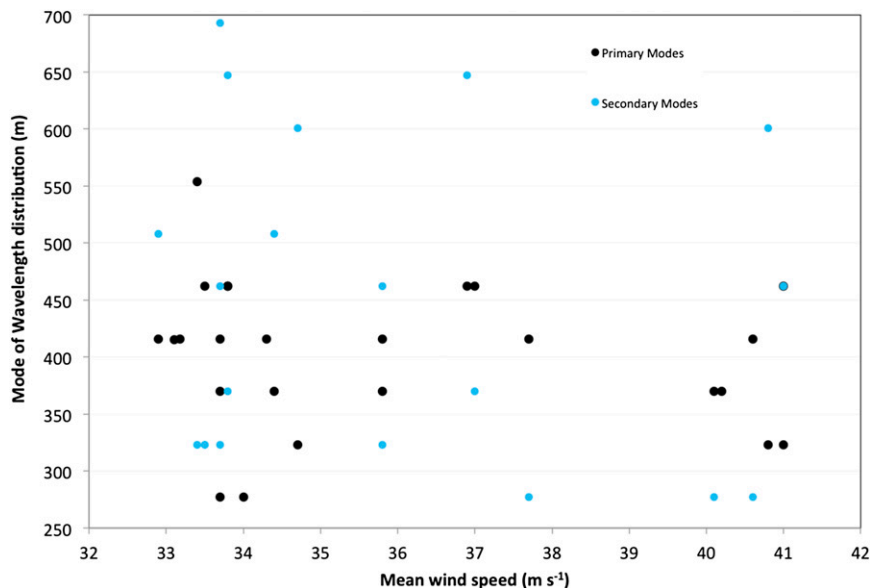
FIG. 11. Mode of wavelength (m) as a function of total horizontal wind speed (m s^{-1}). The most frequently occurring wavelength is indicated by the black dots and, if present, the second most commonly occurring wavelength is indicated by the blue dots. There is little correlation between the horizontal wind speed and the dominant wavelength ($r = -0.16$).

that number by 2. The perturbation horizontal wind speed was calculated by dividing the amplitude between successive peaks and troughs by 2. Figure 9 depicts the cumulative wavelength distribution, binned in 50-m increments, derived from the FFT analysis. At $z = 100$ m ARL, wavelengths ranged in size from 272 to 1498 m, with the most frequently occurring wavelength of 499 m. Using the peak-to-trough method, the most frequently occurring wavelength at $z = 100$ m was 428 m (Fig. 10).[7] At 400 m ARL, the features had a more cellular and less linear appearance, yielding a most frequently occurring wavelength of 610 m (FFT) and 462 m (peak-to-trough), though the frequency of occurrence at 508 m from the peak-to-trough retrieval was nearly identical. This is consistent with the visual appearance of a change in shape of the features with height evident in the dual-Doppler horizontal wind field analyses (Figs. 5 and 6). The characteristic size values extracted from the peak-to-trough analysis are slightly smaller than the values extracted from the FFT analysis, but are roughly comparable and exhibit a similar trend of increasing size with increasing height ARL. The differences between the results from the two analysis methods may be due to the finer length quantization afforded in the peak-to-trough method, potentially better capturing the smaller wavelength

features. Both analysis methods yield most common wavelengths that are comparable to the 350–500-m mean wavelengths documented in the single Doppler analyses of L08 and K13b, and are consistent with the ~500-m wavelength reported in WW98, and the current analysis documents broadening of features with height documented by L08. The most frequently occurring wavelength was not well correlated with the domain average total horizontal wind speed ($r = -0.16$), for the range of horizontal wind speeds (~33 to ~41 m s^{-1}) observed (Fig. 11) and no systematic change in wavelength was detected with time ($r = -0.17$) (Fig. 12).

The wavelengths of the rolls leeward and windward of the barrier island were compared at $z = 100$ m ARL and, while the FFT analysis yielded no significant differences in the characteristic size (Fig. 13), the peak-to-trough analysis revealed a decrease in the most frequently occurring wavelength from 462 m windward to 370 m leeward of the barrier island (Fig. 14). Again, the peak-to-trough method may capture more of the smaller-scale perturbations, which accounts for these differing results, and may more accurately characterize the dominant wavelengths. Thus, there is evidence that the brief change in the underlying surface roughness did impact the characteristic size of the HBLRs. Wurman et al. (2013) suggest that the wind speeds very near the surface are affected significantly by large structures on the barrier island outside of the current dual-Doppler analysis domain.

---

[7] Although not included in the plotted histograms, each analysis method also revealed structures with wavelengths less than 200 m.
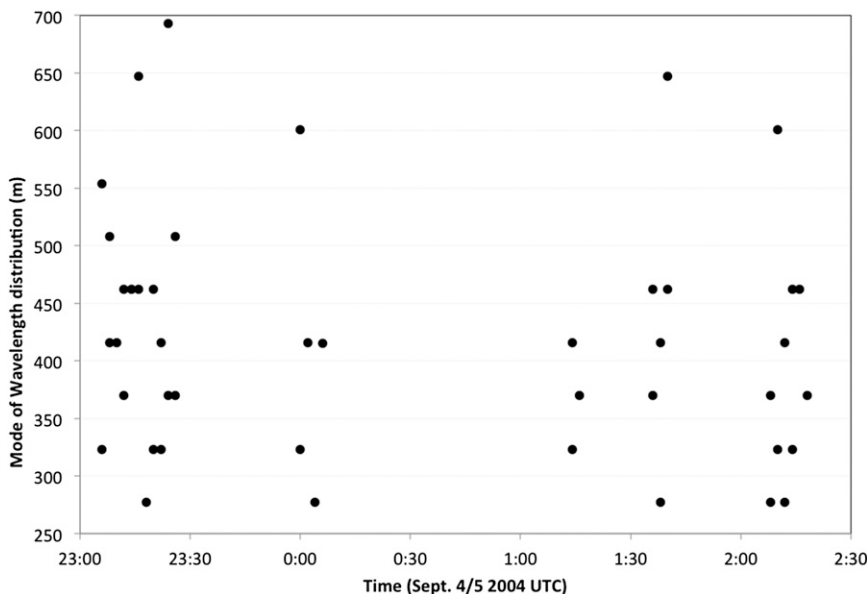
FIG. 12. Mode of wavelength (m) as a function of time. There is little correlation between the horizontal wind speed and the dominant wavelength ($r = -0.17$).

The average amplitude of the horizontal perturbations, calculated from the perturbations obtained from the peak-to-trough analysis, at 100 (400) m ARL, was approximately 1.7 (1.4) m s^{-1}, but the amplitudes were highly variable, with a standard deviation of 1.3 m s^{-1}. The amplitudes of the horizontal perturbation velocities were positively correlated with the wavelength ($r = 0.58$ at 100 m and $r = 0.56$ at 400 m) and, in particular, at larger wavelengths, the lower bound on the perturbation wind speed increases (Fig. 15). Therefore, analyses that focus on the larger, kilometer-scale features may not capture the full spectrum of intensities associated with the subkilometer HBL structures.

2) SHAPE

The analyses show a change in the shape of the coherent structures with height (Figs. 5 and 6). Additionally, both the FFT and the peak-to-trough analysis of wavelength reveal a larger characteristic wavelength at the higher levels. To assess this change in shape, a two-dimensional autocorrelation was calculated at $z = 50/100$ m and $z = 400$ m ARL for the horizontal perturbation wind speeds in the rainbands and eyewall (Fig. 16). The two-dimensional autocorrelation results suggest a linear morphology at $z = 50/100$ m ARL and a more cellular morphology at $z = 400$ m ARL. Explicit determination of the cause of differences in structure at 50/100 m from that at 400 m was not possible from the current analysis. However, it is likely that the wind field at lower elevations is strongly influenced by friction

while the flow aloft is more sensitive to the deeper shear profile and the stability of the HBL.

3) VERTICAL MOMENTUM FLUX AND TURBULENT KINETIC ENERGY

With the three components of the perturbation winds derived from the dual-Doppler analysis, there is enough information to calculate directly the turbulent momentum flux, $\tau = (\overline{u'w'}^2 + \overline{v'w'}^2)^{1/2}$, by the HBLRs. In the HBLR conceptual model (e.g., WW98; M05), the downward branches transport relatively higher horizontal momentum ($w' < 0$; u' and $v' > 0$) while the reverse
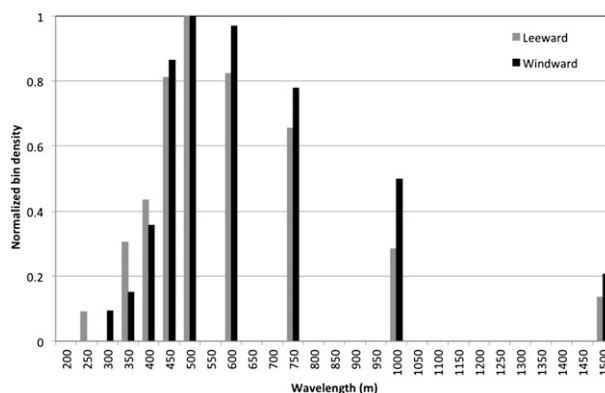
FIG. 13. Distribution of wavelength present in the dual-Doppler wind syntheses for all dual-Doppler times at $z = 100$ m ARL leeward (gray) and windward (black) of the barrier island using an FFT analysis. There is no change in the most frequently occurring wavelength (499 m) as a function of location relative to the barrier island.
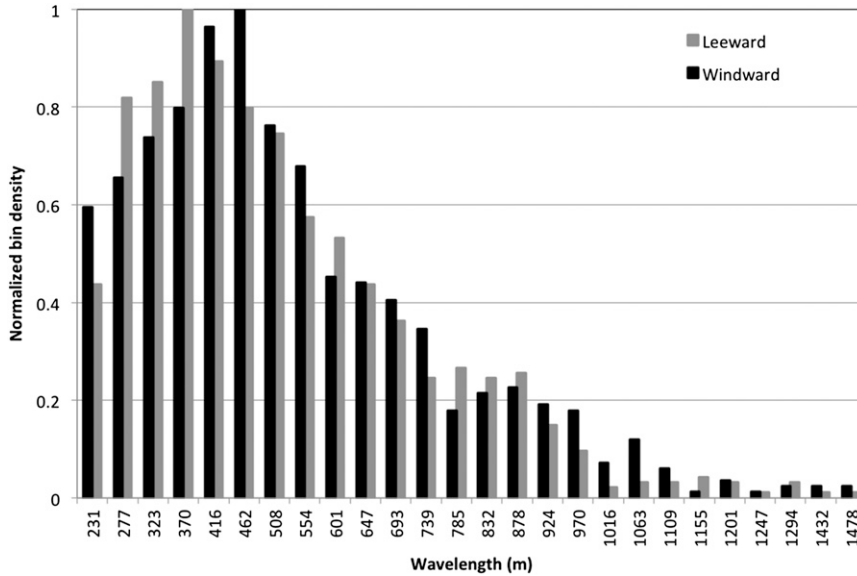
FIG. 14. Distribution of wavelength present in the dual-Doppler wind syntheses for all dual-Doppler times at $z = 100$ m ARL leeward (gray) and windward (black) of the barrier island using the peak-to-trough method. There is a change in the most frequently occurring wavelength as a function of location relative to the barrier island. The mode wavelength windward is 462 m and leeward is 370 m.

occurs in the upward branches (i.e., when $w' > 0$; u' and $v' < 0$). So, $u'w'$ and $v'w' < 0$ over individual rolls and averaged over the entire domain. Because of the incomplete sampling of transient and rapidly evolving roll features discussed above (see Fig. 8), a meaningful domain-wide calculation of the vertical momentum flux is precluded. However, vertical momentum flux can be calculated over individual, well-sampled and retrieved, rolls. For example, at 0004 UTC, the perturbation horizontal wind speed and vertical wind velocities associated
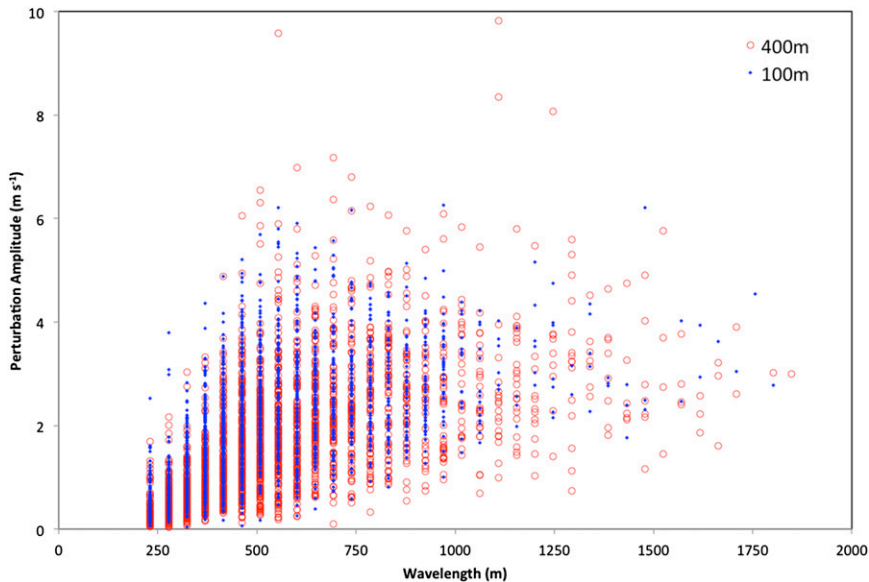
FIG. 15. Amplitude of the perturbation velocity (m s^{-1}) as a function of wavelength (m) for $z = 100$ m ARL (blue) and $z = 400$ m ARL (red) for all dual-Doppler volumes. As the wavelength increases, the minimum perturbation amplitude also increases ($r = 0.58$ at 100 m ARL and $r = 0.56$ at 400 m ARL).
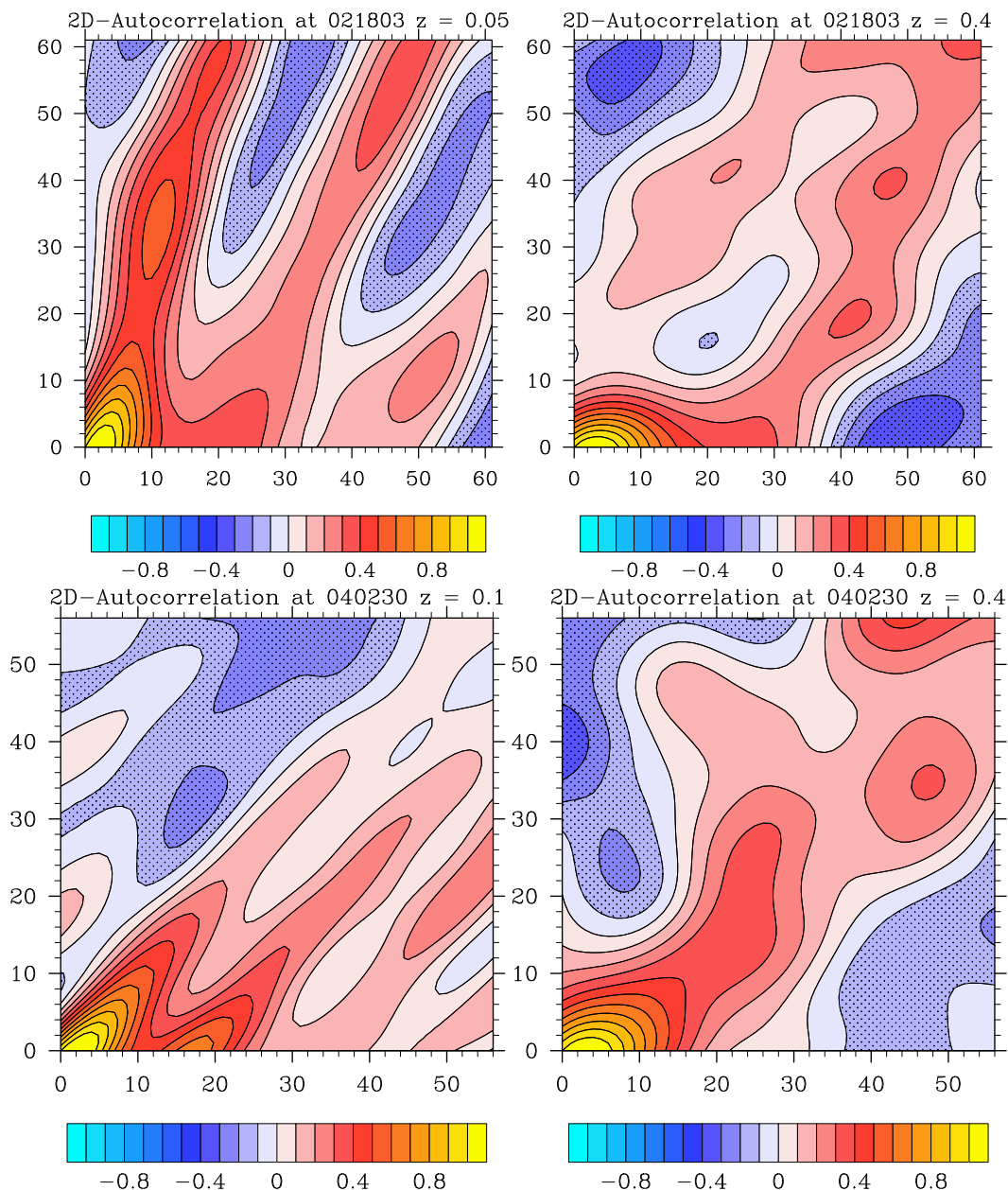
FIG. 16. Two-dimensional autocorrelation of the horizontal perturbation wind speed at z = (left) (top) 50 and (bottom) 100 m ARL, and (right) z = 400 m ARL for a subset of the dual-Doppler domain at (top) 0218:03 and (bottom) 0402:30 UTC. Features have a linear correlation at z = 50 (100) m and a more cellular correlation at z = 400 m.

with a HBLR (Fig. 17) were well correlated at 100 m ARL (r = −0.47). The maximum downward vertical momentum flux through 100 m ARL associated with the HBLCS shown in Fig. 17 was 11.9 m² s⁻². The 11.9 m² s⁻² value is comparable to the results of M05, who derived the momentum flux over individual rolls using three-dimensional wind estimates from single-Doppler data, and is approximately 2–3 times larger than the vertical

momentum transport typically used in homogeneous turbulent parameterization schemes (M05). However, given the overall low negative correlation between the horizontal perturbation wind speed and vertical motion, possibly due to the transience of the strongest roll perturbations, the present calculation over a single roll feature as well as that of M05 may overestimate area average vertical momentum flux.
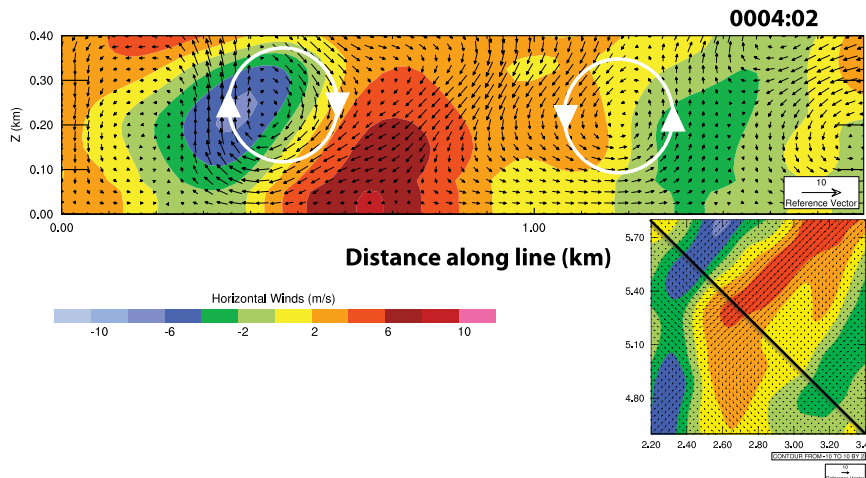
FIG. 17. Example vertical cross section perpendicular to a roll where the perturbation horizontal wind speed and vertical winds are correlated. There is a net downward vertical momentum flux at 100 m ARL that approaches $11.6 \, \mathrm{m^2 \, s^{-2}}$ in the roll. The correlation between the vertical winds and the horizontal perturbation winds decreases above 100 m ARL.

Another measure of turbulent intensity within the HBL is the TKE. TKE was calculated for each level at each time in the dual-Doppler syntheses using the following relationship:

$$\mathrm{TKE} = 0.5 \sum_N (\overline{u'^2} + \overline{v'^2} + \overline{w'^2}),$$

where $\overline{u'}$, $\overline{v'}$, and $\overline{w'}$ are the spatially averaged perturbation wind components in the x, y, and z directions, respectively, and N is the number of points included in the spatial average. The perturbation velocities were averaged over a 200 m × 200 m horizontal area, which corresponds to approximately eight samples in any horizontal direction. The median TKE value was then computed at each analysis level for a representative 2.5 km × 2.5 km subdomain, yielding a vertical TKE profile (Fig. 18). Domain-averaged TKE values were comparable to, albeit slightly larger than, those values derived in the single-Doppler radar analyses of L10 (largest value in the HBL was $16 \, \mathrm{m^2 \, s^{-2}}$) and Rogers et al. (2012), as well as the in situ airborne measurements reported by Zhang et al. (2011). There was a substantial spread in the TKE values at different points across subdomain, however, depending on where the TKE profile was generated relative to the coherent structures (Fig. 19). TKE values approaching $30 \, \mathrm{m^2 \, s^{-2}}$ were found in some of the coherent structures (Fig. 19, right), illustrating the importance of sampling in the TKE calculations. These larger values of TKE were similar to the LES results of Hurricane Ivan landfall (Zhu 2008), which yielded characteristic TKE values of approximately $20 \, \mathrm{m^2 \, s^{-2}}$. For the majority of the TKE analyses,

there is a decrease in TKE between approximately 50 and 150 m ARL, and then again an increase in TKE to the top of the domain. It is possible that 150–200 m ARL delineates the top of the frictional inflow layer (or some other boundary in the HBL) since the coherent structures also increase in size and change shape above this level. TKE values were correlated with the mean total horizontal wind speed ($r = 0.63$), and above mean horizontal wind speeds of $40 \, \mathrm{m \, s^{-1}}$ there is a large spread in the TKE values (Fig. 20). This large spread in TKE values above $40 \, \mathrm{m \, s^{-1}}$ primarily reflects an increase in height, which was associated with a larger spread of perturbation winds (Fig. 15).

4. Discussion and conclusions

The dual-Doppler analyses revealed the finescale three-dimensional vector-wind field structure of the landfalling HBL. Coherent structures were present through the depth of the analysis domain and updraft/downdraft pairs were observed. Differences were observed in the mode wavelength, characteristic shape and TKE values between coherent structures very near the surface ($z = 100 \, \mathrm{m}$ ARL) and those aloft ($z = 400 \, \mathrm{m}$ ARL). It is likely that surface friction predominantly influences the low level structures, while processes aloft influence structures at higher levels. Also, in the inner eyewall and eye of the hurricane, the HBL structures, even at low levels, lost linear coherency. Since the wind speeds observed in these regions were still large, this loss of linear coherency was likely due to a change in stability associated with the inner eyewall and eye. Indeed,
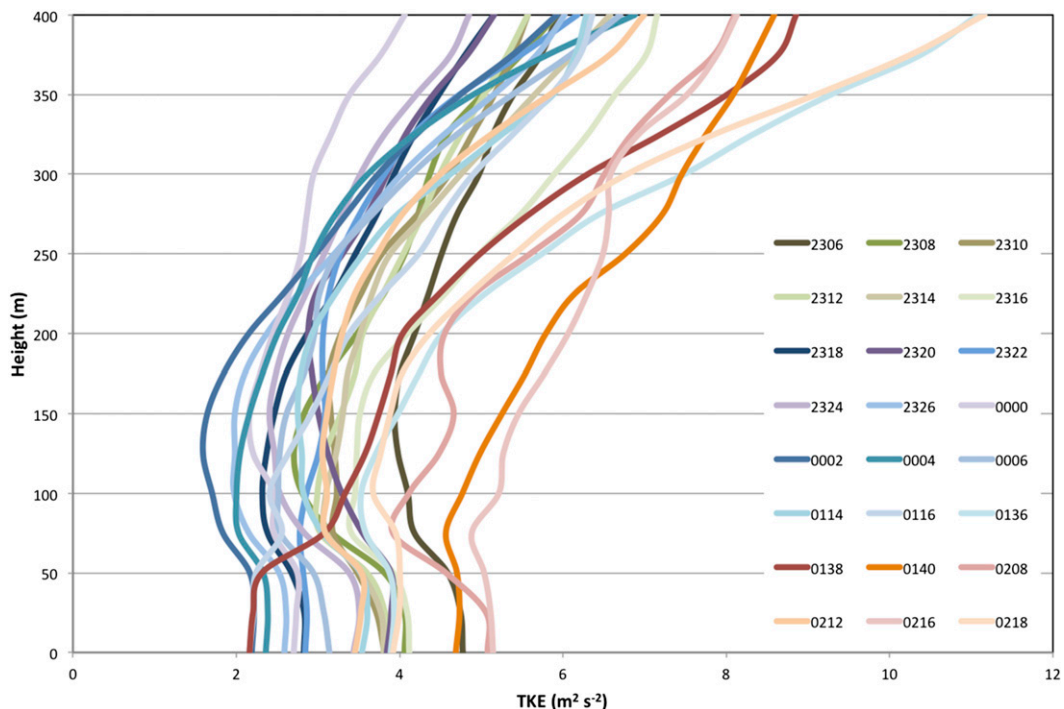
FIG. 18. The median TKE as a function of height for dual-Doppler analyses during the 2306–0218 UTC time period. For all times there is an increase in TKE above approximately $z = 100$–200 m ARL.

WW98 noted a similar change in HBLCSs as the eye made landfall.

HBLCSs, with similar characteristics to roll circulations, were correlated with perturbations in horizontal momentum, resulting in strong vertical flux of horizontal momentum. While the flux values in individual circulations were near $12 \, \mathrm{m^2 \, s^{-2}}$, 2–3 times higher than those used in turbulence parameterization schemes (M05), the domain-wide average of vertical flux of horizontal momentum is much lower due a small domain-wide
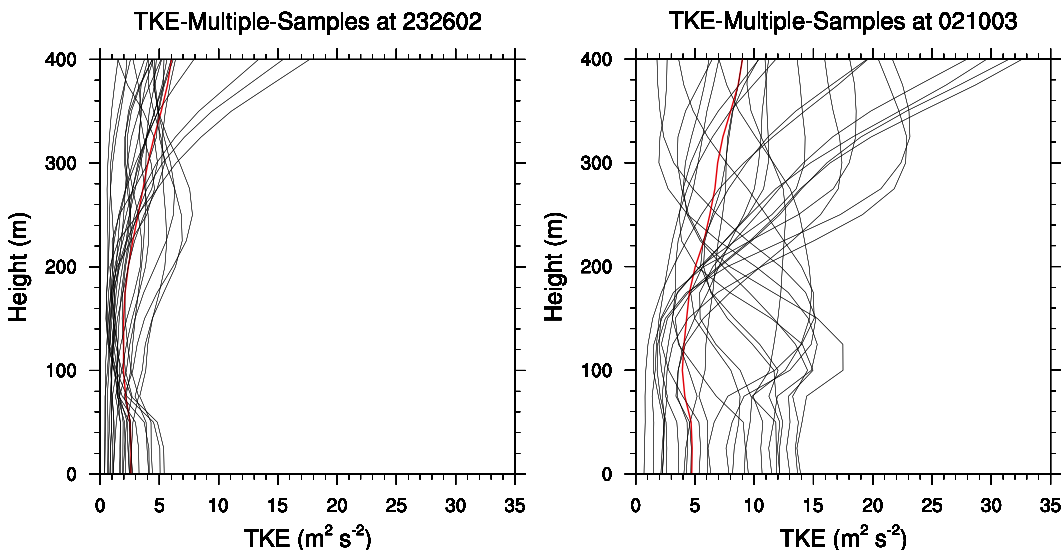
FIG. 19. Examples of the range of TKE values that can occur within the dual-Doppler domain for the (left) 2326 UTC analysis and (right) 0210 UTC analysis. Select values at random grid points within the domain are shown in black and the median value for all grid points in the domain is shown in red.
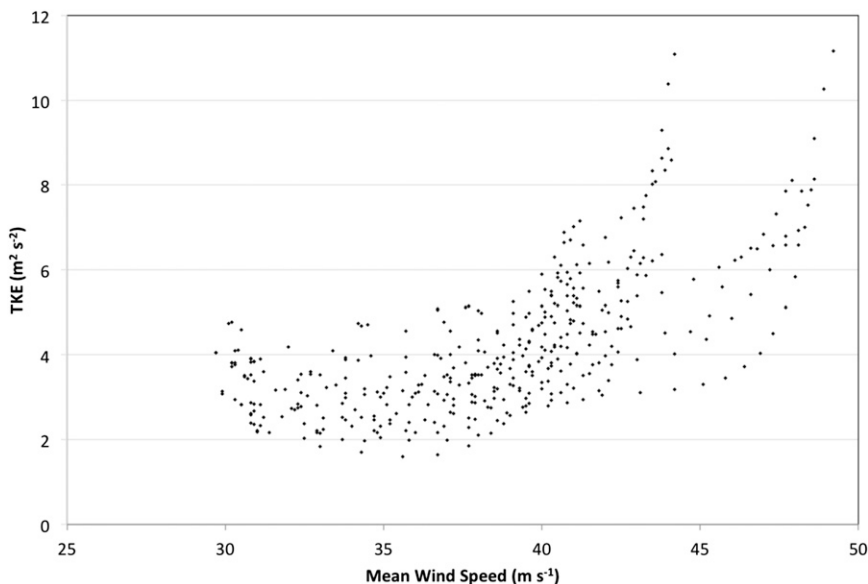
FIG. 20. TKE as a function of mean horizontal wind speed for all heights. TKE and mean horizontal wind speed are well correlated ($r = 0.63$). Above approximately $40 \, \mathrm{m \, s^{-1}}$, there is a large spread in the TKE values, which is primarily due to variations in wind speed with height.

correlation coefficient between w' and the perturbation wind speed ($r = -0.25$ to -0.36). This is likely an artifact of limitations of the dual-Doppler vertical velocity retrievals and a manifestation of the transient nature of the intense perturbations in the coherent structures, where only a fraction of each of the quasi-linear streak features is associated with the maximum intensity vertical motions at any given time. Current turbulence parameterizations are closer to the current area-averaged results.

Domain-wide TKE values were slightly larger than the open-ocean airborne radar-derived values of L10 and Rogers et al. (2012), indicating that values closer to the surface and/or resolution of the small-scale features, and/or surface interactions at landfall have a detectable effect on TKE in the HBL. As such the TKE values derived in the current study were closer in magnitude to the LES results of Zhu (2008) of Hurricane Ivan landfall, particularly in the HBLCSs. Moreover, TKE analyses at individual grid points indicate a large spread in values across the dual-Doppler domain, suggesting the dropsonde analyses may not fully represent the turbulent processes within the HBL. Even though the perturbation velocities are shown to be somewhat proportional to average horizontal wind speed, much of the difference in the reported results is likely due to differences in methodology, and whether the average perturbation is calculated objectively or is calculated subjectively across selected exemplary coherent vortical structures.

More finescale data and deeper dual-Doppler volumes over a variety of surfaces are needed to confirm the validity of these relationships. Additionally, data obtained at multiple levels simultaneously, such as can be obtained with the rapid-scan DOW (Wurman 2003), reducing sampling errors due to rapid evolution of the most intense portions of the HBLCSs, are needed to characterize the domain-wide vertical momentum fluxes.

REFERENCES

Barnes, S. L., 1964: A technique for maximizing details in numerical weather map analysis. *J. Appl. Meteor.,* **3,** 396–409, doi:10.1175/1520-0450(1964)003<0396:ATFMDI>2.0.CO;2.

Braun, S. A., and W. K. Tao, 2000: Sensitivity of high-resolution simulations of Hurricane Bob (1991) to planetary boundary layer parameterizations. *Mon. Wea. Rev.,* **128,** 3941–3961, doi:10.1175/1520-0493(2000)129<3941:SOHRSO>2.0.CO;2.

Carbone, R. E., M. J. Carpenter, and C. D. Burghart, 1985: Doppler radar sampling limitations in convective storms. *J. Atmos. Oceanic Technol.,* **2,** 357–361, doi:10.1175/1520-0426(1985)002<0357:DRSLIC>2.0.CO;2.

Foster, R. C., 2005: Why rolls are prevalent in the hurricane boundary layer. *J. Atmos. Sci.,* **62,** 2647–2661, doi:10.1175/JAS3475.1.

Franklin, J. L., R. J. Pasch, L. A. Avila, J. L. Beven, M. B. Lawrence, S. R. Stewart, and E. S. Blake, 2006: Atlantic hurricane season of 2004. *Mon. Wea. Rev.,* **134,** 981–1025, doi:10.1175/MWR3096.1.

Hill, K. A., and G. M. Lackmann, 2009: Analysis of idealized tropical cyclone simulations using the Weather Research and Forecasting model: Sensitivity to turbulence parameterization and grid spacing. *Mon. Wea. Rev.,* **137,** 745–765, doi:10.1175/2008MWR2220.1.

Kepert, J. D., 2012: Choosing a boundary layer parameterization for tropical cyclone modeling. *Mon. Wea. Rev.,* **140,** 1427–1445, doi:10.1175/MWR-D-11-00217.1.

Koch, S. E., M. desJardins, and P. J. Kocin, 1983: An interactive Barnes objective map analysis scheme for use with satellite and conventional data. *J. Climate Appl. Meteor.,* **22,** 1487–1503, doi:10.1175/1520-0450(1983)022<1487:AIBOMA>2.0.CO;2.

Kosiba, K. A., J. Wurman, P. Markowski, Y. Richardson, P. Robinson, and J. Marquis, 2013a: Genesis of the Goshen County, Wyoming, tornado on 5 June 2009 during VORTEX2. *Mon. Wea. Rev.,* **141,** 1157–1181, doi:10.1175/MWR-D-12-00056.1.

——, ——, F. Master, and P. Robinson 2013b: Mapping of near-surface winds in Hurricane Rita using fine-scale radar, anemometer, and land-use data. *Mon. Wea. Rev.,* **141,** 4337–4349, doi:10.1175/MWR-D-12-00350.1.

Lorsolo, S., J. L. Schroeder, P. Dodge, and F. Marks, 2008: An observational study of hurricane boundary layer small-scale coherent structures. *Mon. Wea. Rev.,* **136,** 2871–2893, doi:10.1175/2008MWR2273.1.

——, J. A. Zhang, F. D. Marks Jr., and J. Gamache, 2010: Estimation and mapping of hurricane turbulent energy using airborne Doppler measurements. *Mon. Wea. Rev.,* **138,** 3656–3670, doi:10.1175/2010MWR3183.1.

Majcen, M., P. Markowski, Y. Richardson, D. Dowell, and J. Wurman, 2008: Multipass objective analyses of Doppler radar data. *J. Atmos. Oceanic Technol.,* **25,** 1845–1858, doi:10.1175/2008JTECHA1089.1.

Moeng, C.-H., J. Dudhia, J. Klemp, and P. Sullivan, 2007: Examining two-way grid nesting for large eddy simulation of the PBL using the WRF model. *Mon. Wea. Rev.,* **135,** 2295–2311, doi:10.1175/MWR3406.1.

Morrison, I., S. Businger, F. Marks, P. Dodge, and J. A. Businger, 2005: An observational case for the prevalence of roll vortices in the hurricane boundary layer. *J. Atmos. Sci.,* **62,** 2662–2673, doi:10.1175/JAS3508.1.

Pauley, P. M., and X. Wu, 1990: The theoretical, discrete, and actual response of the Barnes objective analysis scheme for one- and two-dimensional fields. *Mon. Wea. Rev.,* **118,** 1145–1164, doi:10.1175/1520-0493(1990)118<1145:TTDAAR>2.0.CO;2.

Rogers, R., S. Lorsolo, P. Reasor, J. Gamache, and F. Marks, 2012: Multiscale analysis of tropical cyclone kinematic structure from airborne Doppler radar composites. *Mon. Wea. Rev.,* **140,** 77–99, doi:10.1175/MWR-D-10-05075.1.

Wurman, J., 2001: The DOW mobile multiple Doppler network. Preprints, *30th Int. Conf. on Radar Meteorology,* Munich, Germany, Amer. Meteor. Soc., 95–97.

——, 2003: Preliminary results from the rapid-scan DOW: A multibeam inexpensive alternative to phased arrays. Preprints, *31st Conf. on Radar Meteorology,* Seattle, WA, Amer. Meteor. Soc., 11B.1. [Available online at https://ams.confex.com/ams/32BC31R5C/techprogram/paper_63866.htm.]

——, and J. Winslow, 1998: Intense sub-kilometer boundary layer rolls in Hurricane Fran. *Science,* **280,** 555–557, doi:10.1126/science.280.5363.555.

——, J. M. Straka, E. N. Rasmussen, M. Randall, and A. Zahrai, 1997: Design and deployment of a portable, pencil-beam, pulsed, 3-cm Doppler radar. *J. Atmos. Oceanic Technol.,* **14,** 1502–1512, doi:10.1175/1520-0426(1997)014<1502:DADOAP>2.0.CO;2.

——, K. Kosiba, P. Robinson, and F. J. Masters, 2013: Fine-scale dual-Doppler and in situ observations of the hurricane boundary layer in Hurricane Isaac (2012). *Extended Abstracts, 36th Conf. on Radar Meteorology,* Breckenridge, CO, Amer. Meteor. Soc., 184. [Available online at https://ams.confex.com/ams/36Radar/webprogram/Paper229319.html.]

Zhang, J. A., K. B. Katsaros, P. G. Black, S. Lehner, J. R. French, and W. M. Drennan, 2008: Effects of roll vortices on turbulent fluxes in the hurricane boundary layer. *Bound.-Layer Meteor.,* **128,** 173–189, doi:10.1007/s10546-008-9281-2.

——, F. D. Marks, M. T. Montgomery, and S. Lorsolo, 2011: An estimation of turbulent characteristics in the low-level region of intense hurricanes Allen (1980) and Hugo (1989). *Mon. Wea. Rev.,* **139,** 1447–1462, doi:10.1175/2010MWR3435.1.

Zhu, P., 2008: Simulation and parameterization of the turbulent transport in the hurricane boundary layer by large eddies. *J. Geophys. Res.,* **113,** D17104, doi:10.1029/2007JD009643.